A Paradigm for Path Following Control of a Ribbon-Fin Propelled Biomimetic Underwater Vehicle

Rui Wang, Shuo Wang, Yu Wang, Min Tan, and Junzhi Yu, *Senior Member, IEEE*

***Abstract*—This paper addresses the problem of path following for biomimetic underwater vehicles (BUVs) propelled by undulatory ribbon-fins. First, the general kinematics and dynamics models of underwater vehicles are presented, followed by a fuzzy logic model for dealing with a nonlinear relationship between the propulsive force/torque and the control parameters of the undulatory fins of the BUV. Then the path following problem of the BUV is formulated. A path following control paradigm integrating the line-of-sight guidance system with backstepping (BP) technique is proposed to maneuver the BUV to follow a predefined parameterized curve without time constraints. The stability of the BP controller is analyzed and guaranteed by Lyapunov stability theory. Finally, simulations and experimental results illustrate the performance of the proposed path following control paradigm.**

***Index Terms*—Backstepping (BP), biomimetic underwater vehicle (BUV), line-of-sight (LOS) guidance, path following, ribbon-fin, undulatory propulsion.**

I. Introduction

VARIOUS autonomous underwater vehicles (AUVs) have been proposed for numerous applications in marine and military fields, such as underwater operation, military reconnaissance, leakage detection, and so forth [1]–[5]. Nevertheless, as operations in dangerous and worse underwater environments become more common and complicated, biomimetic underwater vehicles (BUVs) propelled by undulatory fins have received much attention, whose appealing nature involves stronger disturbance rejection, more remarkable maneuverability, and quieter actuation than conventional underwater vehicles equipped with axial propellers [6], [7].

Manuscript received February 8, 2017; accepted May 9, 2017. Date of publication June 5, 2017; date of current version February 14, 2019. This work was supported in part by the National Natural Science Foundation of China under Grant 61233014 and Grant 61333016, in part by the Foundation for Innovative Research Groups of the National Natural Science Foundation of China under Grant 61421004, and in part by the Beijing Natural Science Foundation under Grant 3141002. This paper was recommended by Associate Editor C.-T. Lin. *(Corresponding author: Shuo Wang.)*

R. Wang and S. Wang are with the State Key Laboratory of Management and Control for Complex Systems, Institute of Automation, Chinese Academy of Sciences, Beijing 100190, China, and also with the University of Chinese Academy of Sciences, Beijing 100049, China (e-mail: shuo.wang@ia.ac.cn).

Y. Wang, M. Tan, and J. Yu are with the State Key Laboratory of Management and Control for Complex Systems, Institute of Automation, Chinese Academy of Sciences, Beijing 100190, China.

Color versions of one or more of the figures in this paper are available online at http://ieeexplore.ieee.org.

Digital Object Identifier 10.1109/TSMC.2017.2705340

For more than ten years, researchers have developed several kinds of BUVs propelled by undulatory fins [8]–[13]. The earliest undulatory-fin device using the parallel bellows actuator was developed by Sfakiotakis with Heriot-Watt University in 2001 [9]. Hereafter, Northwestern University designed a bio-inspired robotic knifefish with an undulatory propulsor [10]. Zhou and Low [11] developed a robotic manta ray named RoMan-II. A squid-like underwater robot mimicking stingrays was proposed by Osaka University [12]. Wei *et al.* [13] designed a robotic cuttlefish, which can rotate with small turning radius and dive or float vertically in water. Meanwhile, some undulatory fin systems have been developed using advanced materials, such as ionic polymer metal composites, which may help to improve the efficiency of the propulsion system [14], [15]. However, most of researchers focus on undulatory fin control, but seldom consider closed-loop motion control (such as path following, etc.), which are of primary importance for most applications [16], for those BUVs.

Over the past few years, the path following control for AUVs or surface ships has received great attention from worldwide researchers [17]–[19] and various control strategies have been proposed, including linear algebra approach [20], adaptive control [21], [22], sliding-mode method [23], [24], and backstepping (BP) control [25]–[27]. Serrano *et al.* [20] presented a linear algebra approach for trajectory tracking of underactuated surface vessels. Antonelli *et al.* [21] proposed an adaptive control law for the end-effector tracking problem of underwater vehicle-manipulator systems. Healey and Lienard [24] designed a sliding mode autopilot for the combined steering, diving, and speed control functions of an underwater vehicle. Do *et al.* [26] developed a nonlinear control strategy to force an underactuated surface ship to follow a predefined path at a desired speed using the BP method. Sun *et al.* [25] proposed a cascaded control system integrating BP control with bio-inspired model for tracking control of a manned submarine vehicle. Some intelligent control algorithms like fuzzy control are usually used in path following of underwater vehicles for that the dynamics of the controlled system need not to be completely known [29], [30]. Guo *et al.* [30] demonstrated the feasibility of applying a sliding mode fuzzy controller to motion control of an AUV.

Most of the above literatures about path following control have achieved good performance demonstrated in numerical simulation with precise mathematical models of vehicles.

But only a few papers have reported their proposed path following methods applied in the actual systems and achieved acceptable performance in experiments, due to model uncertainty and complex hydrodynamics. Moreover, the propulsion modes and control inputs of BUVs with ribbon-fins are quite different from that of AUVs and surface vessels, such that the model uncertainty and hydrodynamic complexity are more challenging for these BUVs and the path following problem become more difficult.

This paper provides a positive effort to the above challenging problem. The preliminary goal of this paper is to develop a close-loop control paradigm for a BUV named RobCutt-II to ensure path following in the underwater space. In order to obtain good low-speed stability, the RobCutt-II adopts undulatory propulsion as its actuation system, which in turn poses challenges to the design of the motion control system. The look-ahead line-of-sight (LOS) guidance law mimicking an experienced sailor is implemented to compute the foresight point the RobCutt-II needs to track currently. Furthermore, the BP methods are most commonly used in the robot control systems [31], [32]. The control algorithm of BP is quite simple, and the system stability is strictly guaranteed by Lyapunov stability theory. Thus, we use the BP controller to output the required propulsive force and moment based on the derived foresight point and state feedback. Moreover, fuzzy logic model is proposed to build the nonlinear relationship between the propulsive force/torque and the control parameters of the undulatory fins of the RobCutt-II. Compared with traditional model-free control methods, such as proportional-integral-differential (PID) technique, we try to make use of the partial model information that can be identified through the combination of BP algorithm and fuzzy logic. Moreover, the integrated design weakens the requirements of BP control for precise model parameters and state feedback. Thus, the proposed control paradigm can be actually applied in the path following control of the RobCutt-II. In the end, we investigate its efficacy through simulations and experiments with a physical prototype.

In the remainder of this paper, the modeling of the RobCutt-II is described in Section II. Section III formulates the path following problem and gives the control paradigm. Section IV details the BP algorithm of the proposed control paradigm. Simulations and experimental results are further provided in Section V. Finally, the conclusion and future work are summarized in Section VI.

II. Modeling of the RobCutt-II

The RobCutt-II presented in this paper is a mechatronic system motivated by the unique undulatory propulsion mode of cuttlefish. The mechanism design is first introduced in this section. Then, the kinematics and dynamics of the RobCutt-II are presented. Finally, the parameter mapping between the propulsive force/torque and the control parameters of the RobCutt-II is built based on fuzzy inference.

A. Design of the RobCutt-II

The mechanical design of the RobCutt-II is based on modular concepts. As shown in Fig. 1, the RobCutt-II is composed of three parts, including a tube-like main body, a five DOF manipulator, and two symmetrically arranged propulsors with fins propulsion. Specially, servo motors for driving the manipulator are installed inside the main body. Those servo motors are connected to the joints of the manipulator by timing belt pulley, gear or wire rope transmission. This concept design significantly reduces the mass of the manipulator and the coupling between the manipulator and the vehicle, which is conductive to the coordinative control and operation in the underwater space [33]. In addition, the propulsor can both swim in the water independently and be used to construct various BUVs propelled by undulatory fins [34].

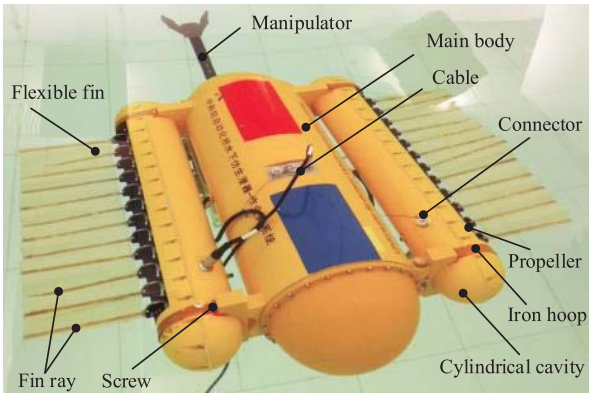

Fig. 1. RobCutt-II prototype.

TABLE I
Structure Parameters of the RobCutt-II Prototype

Parameters	value	Parameters	value
Mass	51.9 kg	Buoyancy	52.1 kg
Manipulator mass	0.889 kg	Main body length	760.6 mm
Main body diameter	260 mm	Cavity length	665 mm
Cavity diameter	120 mm	Fin length	460 mm
Fin width	165 mm	Fin thickness	0.82 mm
Number of fin rays	12	Space of fin rays	43 mm

Table I tabulates the main structure parameters of the RobCutt-II prototype. Since, the buoyancy is approximately equal to the gravity, the RobCutt-II will be neutrally buoyant in the water. Moreover, benefiting from the bilateral symmetrical structure and large metacentric height, the RobCutt-II has good static stability of roll and pitch angles. With the coordinated control of the propagating waves on bilateral fins, the long fins can produce 3-D propulsive force and moment simultaneously. Thus, the RobCutt-II can perform diversified locomotion patterns, including forward/backward swimming, diving/floating motion, and turning maneuver, especially submerging or surfacing vertically. The detailed description about the mechanism design and system configuration of the RobCutt-II can be found in [33]–[35].

B. General Kinematics and Dynamics of Underwater Vehicle

In this paper, the path following issue is addressed in the horizontal plane. It should be mentioned that when swimming

in the 3-D underwater space, the RobCutt-II could first dive or ascend to the desired depth using the method in [13] while maintaining horizontal position, then transits along the horizontal plane to the target. Moreover, the RobCutt-II can switch back to vertical movement mode when the vertical error is larger than a certain threshold.

As previously explained, the RobCutt-II has good stability due to large metacentric height, such that it is reasonable to neglect the motion in pitch and roll. Due to the limitation of motor power of this prototype, the maximum speed of the RobCutt-II is about 0.4 m/s. It is further assumed that the nonlinear damping can be ignored since the linear damping is more significant than the nonlinear damping for BUV moving at low speed. Therefore, the 3 DOF kinematics and dynamics of the vehicle can be represented as (see [36])

$$\begin{aligned} \dot{\eta} &= J(\psi)\nu \\ M\dot{\nu} &= -C(\nu)\nu - D\nu + \tau + \tau_d \end{aligned} \tag{1}$$

where $\eta = [x\ y\ \psi]^T \in \mathbb{R}^3$ represents the earth-fixed position and course, $J(\psi) \in SO(3)$ is the rotational transform matrix from the earth-fixed reference frame to the vehicle-fixed reference frame, $\nu = [u\ v\ r]^T \in \mathbb{R}^3$ represents the vehicle-fixed velocities, M is the inertia matrix including hydrodynamic added inertia, $C(\nu)$ is the coriolis and centripetal matrix, D is the linear damping matrix, $\tau = [\tau_u\ 0\ \tau_r]^T$ is vehicle-fixed propulsive force and moment, where τ_u, τ_r describe the propulsive force and moment acting on surge and yaw, respectively, $\tau_d = [\tau_{du}\ \tau_{dv}\ \tau_{dr}]^T$ describe the disturbance force or moment acting on surge, sway, and yaw. The mass and inertia matrix are assumed to be diagonal matrix. Specifically, the matrices M and D are assumed to have the following structure:

$$M \triangleq \begin{bmatrix} m_{11} & 0 & 0 \\ 0 & m_{22} & 0 \\ 0 & 0 & m_{33} \end{bmatrix},\ D \triangleq \begin{bmatrix} d_{11} & 0 & 0 \\ 0 & d_{22} & 0 \\ 0 & 0 & d_{33} \end{bmatrix}. \tag{2}$$

The particular structure chosen for M and D is motivated by the fact that the RobCutt-II has bilateral symmetry. In this case, the surge mode is decoupled from the sway-yaw subsystem. Moreover, as the motion speed of the RobCutt-II is small, we ignore the nonlinear hydrodynamic damping effect. In addition, although the RobCutt-II fore/aft nonsymmetry implies that the off-diagonal terms of the inertia and damping matrices are nonzero, these terms are small compared to the main diagonal terms because the manipulator mass is far less than the mass of the vehicle [33]. With the particular structure of the inertia matrix M given in (2), the coriolis and centripetal matrix $C(\nu)$ is parameterized as

$$C(\nu) \triangleq \begin{bmatrix} 0 & 0 & -m_{22}v \\ 0 & 0 & m_{11}u \\ m_{22}v & -m_{11}u & 0 \end{bmatrix}. \tag{3}$$

The elements of matrices M, D, and C are calculated as

$$\begin{aligned} m_{11} &= m - X_{\dot{u}}, m_{22} = m - Y_{\dot{v}}, m_{33} = I_z - N_{\dot{r}} \\ d_{11} &= -X_u, d_{22} = -Y_v, d_{33} = -N_r \end{aligned}$$

where m is the mass of the RobCutt-II. The readers may refer to [37] for more details about the definitions of $X_{\dot{u}}$, $Y_{\dot{v}}$, $N_{\dot{r}}$, X_u, Y_v, and N_r.

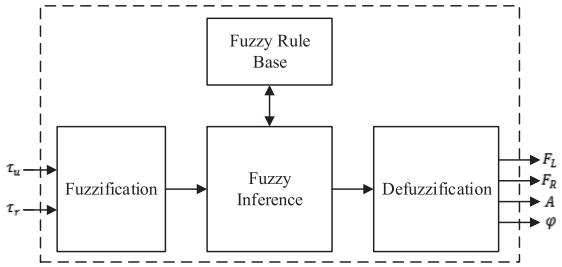

Fig. 2. Block-diagram of the parameter mapping based on fuzzy inference.

C. Modeling of the Propulsors Based on Fuzzy Inference

It is difficult to give a general expression for the quantitative analysis of the fin propulsion that encompasses complex external force and torque due to hydrodynamic force, gravitational force, buoyant force, etc. Although some literatures [38]–[40] try to build hydrodynamic models of the undulatory fins, the limitations of those methods include modeling inaccuracy, parameter identification difficulty, etc. which make it difficult to design the motion control algorithms based on those models of fin propulsion.

To address this challenging problem, fuzzy logic model is proposed to build the nonlinear relationship between the propulsive force/torque and the control parameters of the undulatory fins of the RobCutt-II, i.e., the parameters of propagating waves on bilateral fins including the left fin frequency, the right fin frequency, the amplitude of waves, and the phase difference, which are denoted by F_L, F_R, A, and φ. As shown in Fig. 2, the proposed fuzzy approach has two input and four output: 1) fuzzification; 2) fuzzy inference; 3) fuzzy rule base; and 4) defuzzification are four main components of the fuzzy model.

The fuzzification includes the determination of the universe of discourse of input and output variables, the selections of the fuzzy sets and the membership functions. The universe of discourse of each variable is determined according to the characteristics of undulatory fins and the evaluation of the experimental results of basic motion control : $\tau_u \in [-7, 7]$, $\tau_r \in [-5, 5]$, $F_L \in [-40, 40]$, $F_R \in [-40, 40]$, $A \in [10, 40]$, and $\varphi \in [0, 120]$. In particular, the sign of fin frequency represents the direction of the propagating waves. The fuzzy sets of τ_u, τ_r, A, F_L, F_R, and φ are expressed as T_u, T_r, U_A, U_{F_L}, U_{F_R}, and U_φ, respectively. The sets with seven linguistic values for τ_u, τ_r, F_L, and F_R are defined: $T_u = T_r = U_{F_L} = U_{F_R} = \{NB, NM, NS, Z, PS, PM, PB\}$; the set with four linguistic values for A is defined: $U_A = \{PS, PM, PB, PL\}$; and the set with four linguistic values for φ is defined: $U_\varphi = \{Z, PS, PM, PB\}$. Here, NB, NM, NS, Z, PS, PM, and PB are linguistic values meaning negative large, negative median, negative small, zero, positive small, positive median, and positive large, respectively. In order to simplify the calculation, the standard triangular membership functions is used as illustrated in Fig. 3.

Table II tabulates the specific fuzzy rules base, which is generated on the basis of following two principles.

1) The priority of the heading control are higher than that of the surge control. Namely, when yaw torque and surge

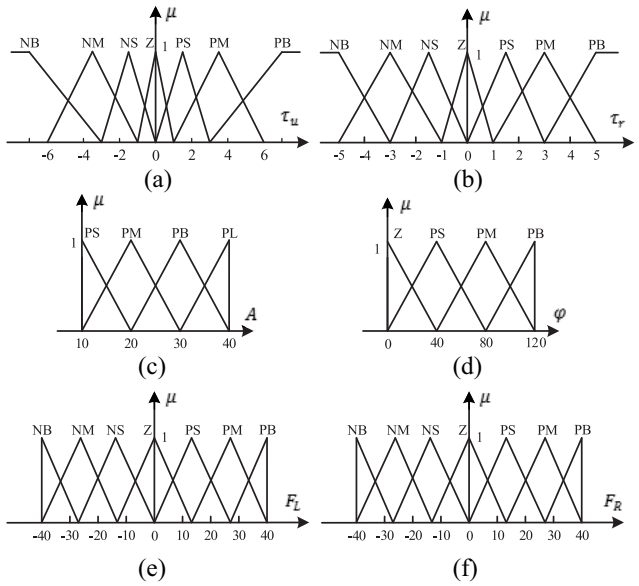

Fig. 3. Membership functions for (a) τ_u, (b) τ_r, (c) A, (d) φ, (e) F_L, and (f) F_R.

TABLE II
FUZZY RULE BASE

$U_{F_L}, U_{F_R}, U_A, U_\varphi$		T_r						
		NB	NM	NS	Z	PS	PM	PB
T_u	NB	NB,PB, PL,PB	NB,NS, PB,PB	NB,NM, PB,PB	NB,NB, PB,PB	NM,NB, PB,PB	NS,NB, PB,PB	PB,NB, PL,PB
	NM	NB,PB, PB,PB	NB,NS, PB,PB	NM,NS, PB,PB	NM,NM, PB,PB	NS,NM, PB,PB	NS,NB, PB,PB	PB,NB, PB,PB
	NS	NB,PB, PB,PB	NM,PM, PB,PB	NM,NS, PM,PM	NS,NS, PS,PS	NS,NM, PM,PM	PM,NM, PB,PB	PB,NB, PB,PB
	Z	NB,PB, PB,PB	NM,PM, PM,PM	NS,PS, PS,PS	Z,Z, Z,Z	PS,NS, PS,PS	PM,NM, PM,PM	PB,NB, PB,PB
	PS	NB,PB, PB,PB	NM,PM, PB,PB	PS,PM, PM,PM	PS,PS, PS,PS	PM,PS, PM,PM	PM,NM, PB,PB	PB,NB, PB,PB
	PM	NB,PB, PB,PB	PS,PB, PB,PB	PS,PM, PB,PB	PM,PM, PB,PB	PM,PS, PB,PB	PB,PS, PB,PB	PB,NB, PB,PB
	PB	NB,PB, PL,PB	PS,PB, PB,PB	PM,PB, PB,PB	PB,PB, PB,PB	PB,PM, PB,PB	PB,PS, PB,PB	PB,NB, PL,PB

force are both large, large yaw torque is guaranteed preferentially.

2) When required yaw torque is small while surge force is large, the direction of waves along the two fins should be consistent but the wave frequency should become different to output large surge force and small yaw torque.

The max–min inference is used for fuzzy inference. Meanwhile, weighted average method is used to achieve defuzzification. We take the computation for the wave frequency of the left fin for an example. The wave frequency of the left fin can be calculated as

$$F_L = \frac{\sum_{i=1}^{m} b_i^{F_L} \mu_i(\tau_u, \tau_r)}{\sum_{i=1}^{m} \mu_i(\tau_u, \tau_r)} \tag{4}$$

where F_L represents the wave frequency of the left fin outputted by fuzzy system, m is the number of fuzzy rules activated by (τ_u, τ_r) as the input, $b_i^{F_L}$ is the membership function center of the output lingual variable of F_L corresponding to the ith rule. $\mu_i(\tau_u, \tau_r)$ represents the membership value of the ith rule, which can be obtained as

$$\mu_i(\tau_u, \tau_r) = \min\left\{\mu_{T_u^j}(\tau_u), \mu_{T_r^k}(\tau_r)\right\} \tag{5}$$

where $\mu_{T_u^j}(\tau_u)$ is the membership value of the jth linguistic value of T_u when the input is τ_u, and $\mu_{T_r^k}(\tau_r)$ is the membership value of the kth linguistic value of T_r when the input is τ_r. Finally, the nonlinear relationship between the propulsive force/torque and the parameters of propagating waves on bilateral fins is built.

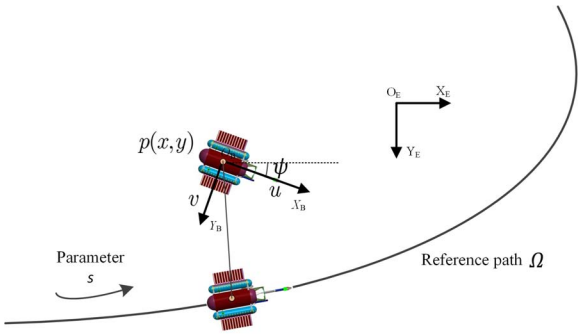

Fig. 4. Schematic of path following for RobCutt-II.

III. PATH FOLLOWING CONTROL PARADIGM

A. Controller Architecture

In the path following task, the vehicle must reach and follow a geometric reference path in the Cartesian space starting from a given initial configuration (on or off the path). The controller is given a geometric description of the assigned Cartesian path. This information is usually available in a parameterized form expressing the desired motion in terms of a path parameter, which may be in particular the arc length along the path. For this task, time dependence is not relevant because one is concerned only with the geometric displacement between the vehicle and the path.

As depicted in Fig. 4, the controller generates control inputs τ_u and τ_r such that the position $p(x, y)$ of the RobCutt-II globally follows a reference path Ω parameterized by $(x_d(s), y_d(s))$ with s being the path parameter at a certain surge speed. In particular, we are interested in designing explicit expressions for τ_u, τ_r such that $\lim_{t\to\infty}[x(t) - x_d(s), y(t) - y_d(s)]^T = 0$ with $u > 0$, for all $t \geq t_0 \geq 0$ and $[x(t_0), y(t_0)]^T \in \mathbb{R}^2$.

In order to solve the above problem, a path following control paradigm is proposed as illustrated in Fig. 5. The integrated control design mainly consists of three parts. The first part is a guidance system based on LOS principle, which is implemented to deduce the foresight point p_{los} the RobCutt-II needs to track currently in real time based on reference path and position feedback. The second part is a BP controller by using foresight point p_{los} and position/orientation feedbacks. In particular, the BP controller outputs propulsive force τ_u and torque τ_r, which are further mapped to the parameter settings of propagating waves on bilateral fins to force the RobCutt-II to converge to the current foresight point p_{los} based on fuzzy inference. A detailed description about the controller design is presented in the later section.

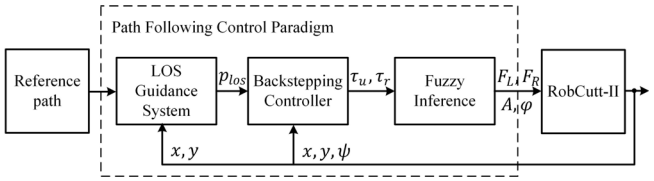

Fig. 5. Block-diagram of the path following controller.

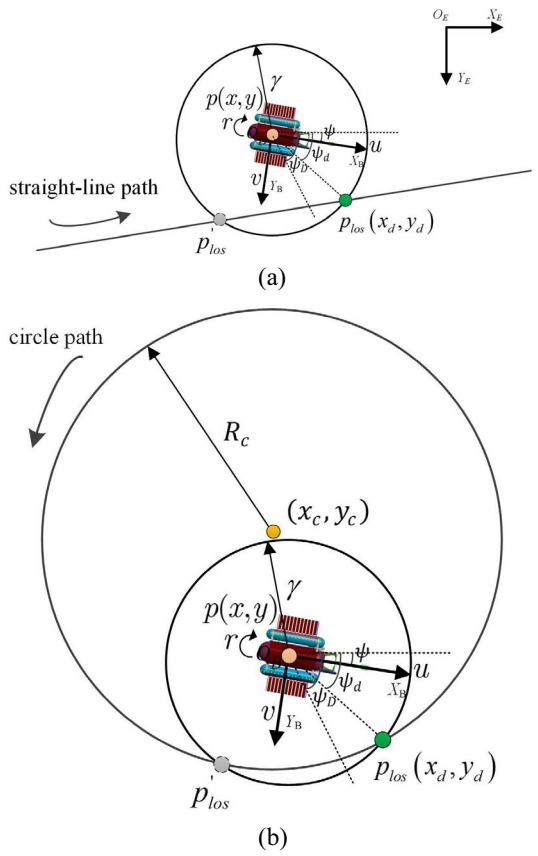

Fig. 6. Modeling of the LOS guidance system. (a) Image sequence of the straight-line path following. (b) Circular path.

B. LOS Guidance System

An LOS guidance system is implemented in the path following control to accomplish motion planning of the BUV. Specially, straight-line and circular paths are considered. The notations of the LOS guidance system are depicted in Fig. 6.

1) $p(x, y)$ and ψ are the real-time position and the heading angle of the RobCutt-II, respectively.
2) γ is the radius of the virtual circle associated with the RobCutt-II.
3) ψ_d is the target heading angle.
4) $p_{\text{los}}(x_d, y_d)$ defines the foresight point.
5) p'_{los} represents the other intersection.

When the path following starts, the controller tries to reduce the cross-track error between the RobCutt-II and the desired path.

Assume that there is a virtual circle associated with the RobCutt-II, whose center is located in the barycenter of the RobCutt-II and the radius is γ. As for the straight-line path, Fig. 6(a) shows that the current foresight point is located somewhere on the straight-line. If the virtual circle intersects the current tracking straight-line path, the intersection point further forward along the path is served as the foresight point, whose coordinate (x_d, y_d) can be calculated by solving

$$(x - x_d)^2 + (y - y_d)^2 = \gamma^2 \tag{6}$$

$$y_d = kx_d + b \tag{7}$$

where k and b are the slope and intercept of the straight line, respectively. Otherwise, the point, which is both on the current tracking straight-line and closest to the virtual circle, is chosen as the foresight point, which can be obtained

$$(x - x_d) + k(y - y_d) = 0 \tag{8}$$

$$y_d = kx_d + b. \tag{9}$$

Analogously, in the case of circular path, as illustrated in Fig. 6(b), if the virtual circle intersects the current tracking circle, the intersection point further forward along the path is chosen as the foresight point, whose position can be derived by solving

$$(x - x_d)^2 + (y - y_d)^2 = \gamma^2 \tag{10}$$

$$(x_d - x_c)^2 + (y_d - y_c)^2 = R_c^2 \tag{11}$$

where (x_c, y_c) and R_c are the center and radius of the circle. Otherwise, the point, which is located both on the current tracking circle and closest to the virtual circle, is selected as the foresight point, which can be deduced from

$$(x - x_c)(y_d - y_c) - (y - y_c)(x_d - x_c) = 0 \tag{12}$$

$$(x_d - x_c)^2 + (y_d - y_c)^2 = R_c^2. \tag{13}$$

Notice that the circle must be centered at the known location of the vehicle in order to compute the coordinates of the intersection points with the straight or circular path. Additionally, the foresight point is related to the current position of the RobCutt-II. That is, the foresight point is changing along with the motion of the RobCutt-II. Next, the BP controller are detailed.

IV. Backstepping Controller

To force the RobCutt-II to converge to the given foresight point, a BP controller is designed in this section. The controller is first derived at the kinematic level by assuming that the control signals are surge speed u and yaw angular velocity r. Then the kinematic controller is extended to the dynamic case.

Let $p_{\text{los}} = (x_d, y_d)$ denote the foresight point, then the target heading angle can be computed as

$$\psi_d = \begin{cases} \pi + \dfrac{1}{2}\text{sgn}(y_e) \cdot \pi, & x_e = 0 \\ \arctan\left(\dfrac{y_e}{x_e}\right) + \pi + \dfrac{1}{2}\text{sgn}(y_e) \cdot \pi & \\ \quad -\dfrac{1}{2}\text{sgn}(x_e)\text{sgn}(y_e) \cdot \pi, & x_e \neq 0 \end{cases} \tag{14}$$

where $x_e = x - x_d$ and $y_e = y - y_d$. $\text{sgn}(\cdot)$ denotes the symbolic function with $\text{sgn}(0) = 1$. In particular, when there is flow disturbance in the path following, using the heading angle ψ_d in the controller would lead to the deviation of the actual

path from the desired path. In order to reduce this static error, heading compensation related to the planar distance error is added to the heading angle in (12). Therefore, the ultimate target heading angle is expressed as

$$\psi_D = \psi_d + c_0 \tanh(c_1 e_{\text{dis}}) \cdot f_{\text{lr}} \tag{15}$$

where ψ_D is the calculated target heading angle with heading compensation for the control to achieve the following, e_{dis} is the distance from the barycenter of the RobCutt-II to the current tracking path. c_0 and c_1 are adjustable parameters. f_{lr} is a sign function defined as follows: $f_{\text{lr}} = 1$, if the RobCutt-II is on the left side of the current tracking path; $f_{\text{lr}} = 0$ if the RobCutt-II is on the current tracking path; and $f_{\text{lr}} = -1$ if the RobCutt-II is on the right side of the current tracking path.

Then, the tracking error can be written as

$$\begin{aligned} x_e &= x - x_d \\ y_e &= y - y_d \\ e_{xy} &= \sqrt{{x_e}^2 + {y_e}^2} \\ \psi_e &= \psi - \psi_D \end{aligned} \tag{16}$$

where ψ_e is heading angle error. Combined with (1), the kinematics equation of motion of the RobCutt-II can be rewritten as

$$\begin{aligned} \dot{e_{xy}} &= -u\cos(\psi_e) + v\sin(\psi_e) \\ \dot{\psi}_e &= r + \frac{\sin(\psi_e)}{e_{xy}}u + \frac{\cos(\psi_e)}{e_{xy}}v. \end{aligned} \tag{17}$$

Feedback control laws for force τ_u and moment τ_r need to be derived to make the equilibrium state of (17) asymptotically stable. Notice that the transformation is only valid for nonzero values of e_{xy}, since the angle ψ_e is undefined for $e_{xy} = 0$. In particular, as for this singularity problem, we guarantee that $e_{xy}(t)$ stays positive for all t so that all mathematical expressions with e_{xy} in the denominator are valid through the selection of the foresight point in the guidance system as mentioned in last section. It should also be mentioned that the transformation (17) is used to display the vehicle kinematics in a form that helps to motivate the derivation of the controller.

With the formulation developed previously, kinematic control is first designed.

Theorem 1: Consider the nonlinear, invariant system described by (1) in closed-loop with the control law

$$\begin{aligned} u &= k_1\big(e_{xy} - \delta\big)\cos^n(\psi_e) \\ r &= -\frac{\cos(\psi_e)}{e_{xy}}v - k_2\psi_e \end{aligned} \tag{18}$$

where e_{xy} and ψ_e are defined in (16), δ is an arbitrary small positive constant, n is a natural number, and $k_2 > k_1 > 0$. Then, for every initial condition $(e_{xy}, \psi_e) \in \mathbb{R}^2$, (e_{xy}, ψ_e) converges to $(\delta, 0)$ as $t \to \infty$.

Proof: Substituting (18) into (17), we can get

$$\begin{aligned} \dot{e_{xy}} &= -k_1\big(e_{xy} - \delta\big)\cos^{n+1}(\psi_e) + v\sin(\psi_e) \\ \dot{\psi}_e &= -k_2\psi_e + k_1\sin(\psi_e)\left(1 - \frac{\delta}{e_{xy}}\right)\cos^n(\psi_e). \end{aligned} \tag{19}$$

It is obvious that $(\delta, 0)$ is an equilibrium point of (e_{xy}, ψ_e). Then we will prove that the equilibrium point is stable based on the Lyapunov's second method for stability [41]. The proof is organized as follows. First, it will be proved that ψ_e converges to zero as $t \to \infty$. Using this result, it will be further shown that $e_{xy} \to \delta$ as $t \to \infty$.

Convergence of ψ_e: Consider the following Lyapunov function candidate:

$$V_1 = \frac{1}{2}{\psi_e}^2. \tag{20}$$

Evaluating its time derivative using (17) yields

$$\dot{V}_1 = \psi_e\dot{\psi}_e = \psi_e\left(r + \frac{\sin(\psi_e)}{e_{xy}}u + \frac{\cos(\psi_e)}{e_{xy}}v\right). \tag{21}$$

In combination with (18) and (19) will allow to get

$$\dot{V}_1 = -{\psi_e}^2\left[k_2 - k_1\frac{\sin(\psi_e)}{\psi_e}\left(1 - \frac{\delta}{e_{xy}}\right)\cos^n(\psi_e)\right]. \tag{22}$$

Since $([\sin(\psi_e)]/\psi_e) < 1$, $(1 - (\delta/e_{xy})) \le 1$, $\cos^n(\psi_e) \le 1$, and $k_2 > k_1 > 0$, thus $\dot{V}_1 \le 0$, and $\dot{V}_1 = 0$ only when $\psi_e = 0$. Then we can conclude that ψ_e is asymptotically stable and converges to zero as $t \to \infty$.

Convergence of e_{xy}: Consider the Lyapunov function candidate

$$V_2 = \frac{1}{2}\big(e_{xy} - \delta\big)^2. \tag{23}$$

Computing its time derivative using (18) yields

$$\begin{aligned} \dot{V}_2 &= \big(e_{xy} - \delta\big)\dot{e_{xy}} = \big(e_{xy} - \delta\big)[-u\cos(\psi_e) + v\sin(\psi_e)] \\ &= \big(e_{xy} - \delta\big)\Big[-k_1\big(e_{xy} - \delta\big)\cos^{n+1}(\psi_e) + v\sin(\psi_e)\Big]. \end{aligned} \tag{24}$$

Since $\psi_e \to 0$ as $t \to \infty$. There exists a limited time t_0, $T \ge t_0 \ge 0$ to obtain

$$\cos^{n+1}(\psi_e) > 0, \quad \forall t \ge T. \tag{25}$$

Therefore

$$\begin{aligned} \dot{V}_2 &= -k_1\big(e_{xy} - \delta\big)^2\cos^{n+1}(\psi_e) + v\sin(\psi_e)\big(e_{xy} - \delta\big) \\ &= -k_1(1-\lambda)\big(e_{xy} - \delta\big)^2\cos^{n+1}(\psi_e) \\ &\quad - k_1\lambda\big(e_{xy} - \delta\big)^2\cos^{n+1}(\psi_e) + v\sin(\psi_e)\big(e_{xy} - \delta\big) \\ &\le -k_1(1-\lambda)\big(e_{xy} - \delta\big)^2\cos^{n+1}(\psi_e) = \dot{V}_2^* \\ &\qquad \forall\big(e_{xy} - \delta\big) \ge \frac{|v\sin(\psi_e)|}{k_1\lambda\cos^{n+1}\psi_e}, 0 < \lambda < 1. \end{aligned} \tag{26}$$

It is obvious that $\dot{V}_2^* = 0$ only if $e_{xy} = \delta$, otherwise $\dot{V}_2^* < 0$. So $\dot{V}_2$ is strictly negative definite. Furthermore, $v\sin(\psi_e) \to 0$ as $\psi_e \to 0$, such that $e_{xy} \to \delta$ as $t \to \infty$. ■

Then, the kinematic control is extended to the dynamic case, where the suitable force and torque to drive the RobCutt-II to follow a desired geometric path are derived from the velocity control inputs.

Let u and r in (18) be the virtual control inputs and α_1 and α_2 the corresponding virtual control laws. Introduce the error variables

$$\beta_1 = u - \alpha_1, \beta_2 = r - \alpha_2. \tag{27}$$

From (1), the differential equations of surge speed and yaw angular velocity can be described as

$$\dot{u} = \frac{1}{m_{11}}(\tau_u + m_{22} v r - d_{11} u)$$
$$\dot{r} = \frac{1}{m_{33}}(\tau_r + (m_{11} - m_{22}) u v - d_{33} r). \quad (28)$$

Consider the function V_1 defined in (17) augmented with the quadratic terms β_1 and β_2, that is

$$V_3 = V_1 + \frac{1}{2}{\beta_1}^2 + \frac{1}{2}{\beta_2}^2. \quad (29)$$

The time derivative of V_3 can be written as

$$\begin{aligned}\dot{V}_3 &= \psi_e \dot{\psi}_e + \beta_1 \dot{\beta}_1 + \beta_2 \dot{\beta}_2 \\ &= -{\psi_e}^2 \left[k_2 - k_1 \frac{\sin(\psi_e)}{\psi_e} \left(1 - \frac{\delta}{e_{xy}}\right) \cos^n(\psi_e) \right] \\ &\quad + \psi_e \beta_2 + \psi_e \frac{\sin(\psi_e)}{e_{xy}} \beta_1 + \beta_1 \dot{\beta}_1 + \beta_2 \dot{\beta}_2. \end{aligned} \quad (30)$$

Let the control law for τ_u, τ_r be chosen as

$$\begin{aligned}\tau_u &= -m_{22} v r + d_{11} u + m_{11} \dot{\alpha_1} - m_{11} \frac{\sin(\psi_e)}{e_{xy}} \psi_e - k_3 \beta_1 \\ \tau_r &= (m_{22} - m_{11}) u v + d_{33} r + m_{33} \dot{\alpha_3} - m_{33} \psi_e - k_4 \beta_2 \end{aligned} \quad (31)$$

where k_3 and k_4 are positive constants. Combining (28), (30), and (31), then

$$\begin{aligned}\dot{V}_3 = -{\psi_e}^2 \left[k_2 - k_1 \frac{\sin(\psi_e)}{\psi_e} \left(1 - \frac{\delta}{e_{xy}}\right) \cos^n(\psi_e) \right] \\ - k_3 \frac{{\beta_1}^2}{m_{11}} - k_4 \frac{{\beta_2}^2}{m_{33}}. \end{aligned} \quad (32)$$

Similarly, $\dot{V}_3$ is strictly negative definite, which shows that the subsystem $(\psi_e, \beta_1, \beta_2)$ is global asymptotically stable. Therefore, the extension of Theorem 1 to the dynamic case follows.

Theorem 2: Consider the nonlinear, invariant system described by (1) and the control law (31). Assume the control gains $k_i, i = 1, 2, 3, 4$, δ are positive constants, $k_2 > k_1 > 0$ and n is a natural number. Let e_{xy} and ψ_e be given as (16), then for every initial condition $(e_{xy}, \psi_e) \in \mathbb{R}^2$, (e_{xy}, ψ_e) converges to $(\delta, 0)$ as $t \to \infty$.

Proof: The convergence of $(\psi_e, \beta_1, \beta_2)$ has been proven in (32), therefore, we only need to prove that $e_{xy} - \delta \to 0$, as $t \to \infty$. Consider Lyapunov function candidate

$$V_4 = \frac{1}{2}\left(e_{xy} - \delta\right)^2. \quad (33)$$

Its time derivative is given by

$$\begin{aligned}\dot{V}_4 &= \left(e_{xy} - \delta\right) \dot{e_{xy}} \\ &= \left(e_{xy} - \delta\right) \left[-k_1 \left(e_{xy} - \delta\right) \cos^{n+1}(\psi_e) + v \sin(\psi_e) \right] \\ &\quad - \beta_1 \left(e_{xy} - \delta\right) \cos(\psi_e). \end{aligned} \quad (34)$$

Since $\psi_e \to 0$ as $t \to \infty$. There exists a limited time $t_0, T \geq t_0 \geq 0$ to obtain

$$\cos^{n+1}(\psi_e) > 0, \quad \forall t \geq T. \quad (35)$$

TABLE III
CONTROLLER PARAMETERS IN SIMULATIONS

k_1	k_2	k_3	k_4	γ	δ	n	c_0	c_1
0.2	1.8	200	7	0.4	0.02	1	0	0

Then

$$\begin{aligned}\dot{V}_4 &= -k_1 \left(e_{xy} - \delta\right)^2 \cos^{n+1}(\psi_e) + v \sin(\psi_e) \left(e_{xy} - \delta\right) \\ &\quad - \beta_1 \left(e_{xy} - \delta\right) \cos(\psi_e) \\ &= -k_1 (1 - \lambda) \left(e_{xy} - \delta\right)^2 \cos^{n+1}(\psi_e) - k_1 \lambda \left(e_{xy} - \delta\right)^2 \\ &\quad \cos^{n+1}(\psi_e) + v \sin(\psi_e) \left(e_{xy} - \delta\right) - \beta_1 \left(e_{xy} - \delta\right) \cos(\psi_e) \\ &\leq -k_1 (1 - \lambda) \left(e_{xy} - \delta\right)^2 \cos^{n+1}(\psi_e) = \dot{V}_4^* \\ &\forall \left(e_{xy} - \delta\right) \geq \frac{\left| v \sin(\psi_e) - \beta_1 \left(e_{xy} - \delta\right) \cos(\psi_e) \right|}{k_1 \lambda \cos^{n+1}(\psi_e)} \\ &0 < \lambda < 1. \end{aligned} \quad (36)$$

Analogously, $\dot{V}_4^*$ is negative definite. As it has been proven that $\psi_e, \beta_1 \to 0$, it can be concluded that $v \sin(\psi_e) - \beta_1 (e_{xy} - \delta) \cos(\psi_e)$ will converge to zero, which means that $(e_{xy} - \delta) \to 0$, i.e., $e_{xy} \to \delta$. Therefore, the whole system is asymptotically stable. ■

V. SIMULATIONS AND EXPERIMENTAL RESULTS

A. Simulations

First, to illustrate the performance of the integrated design of the path following system based on an LOS guidance law and a BP controller, simulations are carried out with the model shown in Section II-B. The model parameters used in the simulations are $m_{11} = 57.5, m_{22} = 61.3, m_{33} = 1.15$, $d_{11} = 53, d_{22} = 58$, and $d_{33} = 3.1$.

1) Straight Path Following: A simple case to follow a straight-line path is studied first. The slope and intercept of the straight line are 1 and -0.5 m, respectively. The RobCutt-II starts at posture (0.5 m, 0.5 m, 0 rad), while the initial velocity is zero. The parameter setting of the path following controller is shown in Table III.

Fig. 7 show the simulation results of the straight line path following. Fig. 7(a) depicts the desired path and the actual trajectory of the RobCutt-II. It is observed that the proposed path following controller is able to force the RobCutt-II to catch up and land on the desired path smoothly with no overshoot. Then, the RobCutt-II moves along the desired path and the tracking error between the desired path and the actual trajectory is small. Fig. 7(b) shows the time evolution of the body-fixed velocity. The actual velocity well follows the virtual velocity given by the kinematic design. Moreover, although the velocity in sway of the RobCutt-II is not controlled, its convergence can also be achieved under the path following controller.

2) Circular Path Following: Then, a typical case to follow a circle is studied. The RobCutt-II starts at posture (0.5 m, 1.5 m, 0 rad) and the initial velocity is zero. The center (x_c, y_c) and radius R_c of the circle are (2 m, 1.5 m) and 1.1 m, respectively. A full circle is considered, namely, the arc length along the path $s = 2\pi R_c$. The same parameter setting

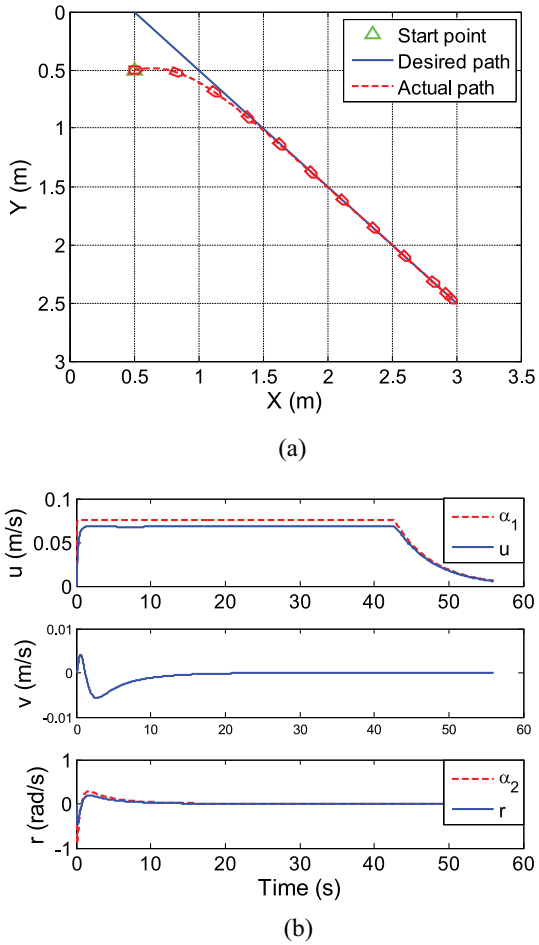

Fig. 7. Simulation results of the straight-line path following. (a) Desired path and actual path. (b) Time evolution of the vehicle-fixed velocity (blue solid line) and virtual velocity (red dotted line).

shown in Table III is used. To reflect the disturbance rejection performance of the controller, zero mean uniform random noises are incorporated into the surge, sway, and yaw dynamics of the RobCutt-II. In addition, a constant flow turbulence, which is unknown from the point of view of the controller, with intensity $V_c = 0.03$ m/s and direction $\phi_c = (33/18)$ rad is also added to the controllers dynamic model.

More detail results based on these conditions are presented in Fig. 8. Fig. 8(a) shows that the RobCutt-II converges to the circle and moves along the desired path. Moreover, the RobCutt-II responds to the disturbance and achieves a satisfactory recovery. Fig. 8(b) shows the time evolution of the vehicle-fixed velocity. The surge speed and yaw angular velocity well follow the virtual control signals derived at the kinematic level while the sway velocity converges to zero under the path following controller. Fig. 8(c) shows the time evolution of the vehicle-fixed propulsive force and moment. All control inputs are bounded. Thus, it can be concluded that the LOS BP controller is practical and effective.

Furthermore, some comparative experiments including BP with no heading compensation, sliding mode control (SMC) [42], and PID control are performed. Fig. 9 shows the simulation results. Specially, The path following can all be achieved as shown in Fig. 9(a). However, it can be seen

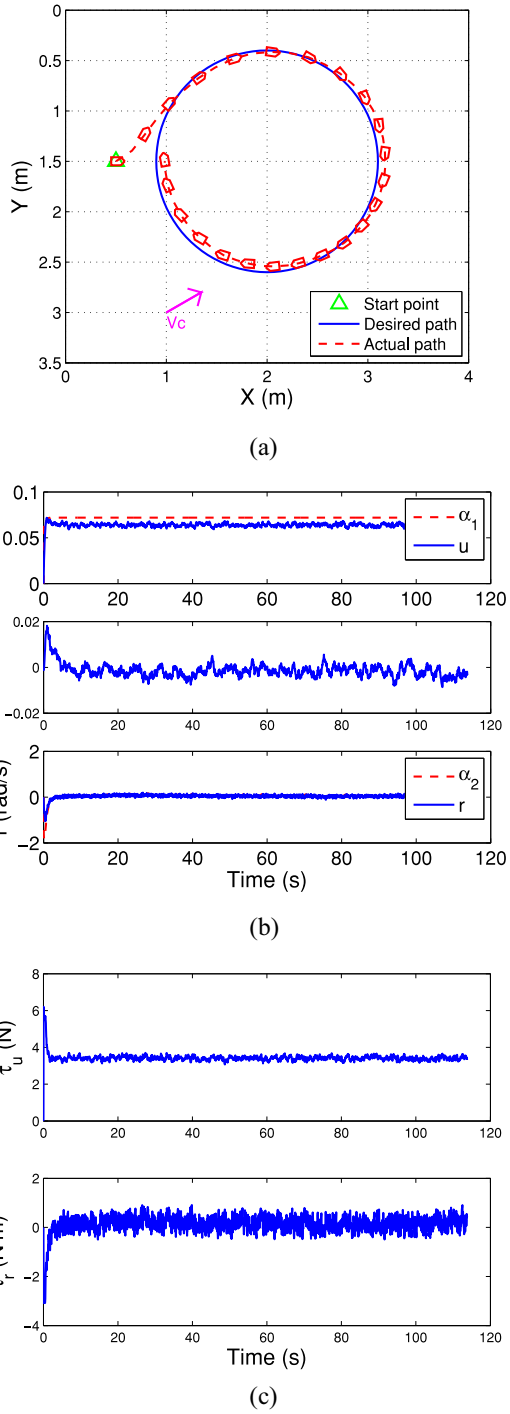

Fig. 8. Simulation results of the circular path following. (a) Circle to be followed and actual path. (b) Vehicle-fixed velocity. (c) Propulsive force and moment.

from Fig. 9(b) that the cross-track error (the shortest distance from the current barycenter of the RobCutt-II to the desired path) with heading compensation is smaller than that without heading compensation in the path following. Specifically, when the RobCutt-II moves along the circle, the maximum cross-track error of the method with heading compensation is 0.0933 m, while the method without heading compensation is 0.1821 m, which indicates that heading compensation shows more precise motion than direct calculation of the orientation for path following of the RobCutt-II. Moreover, the cross-track

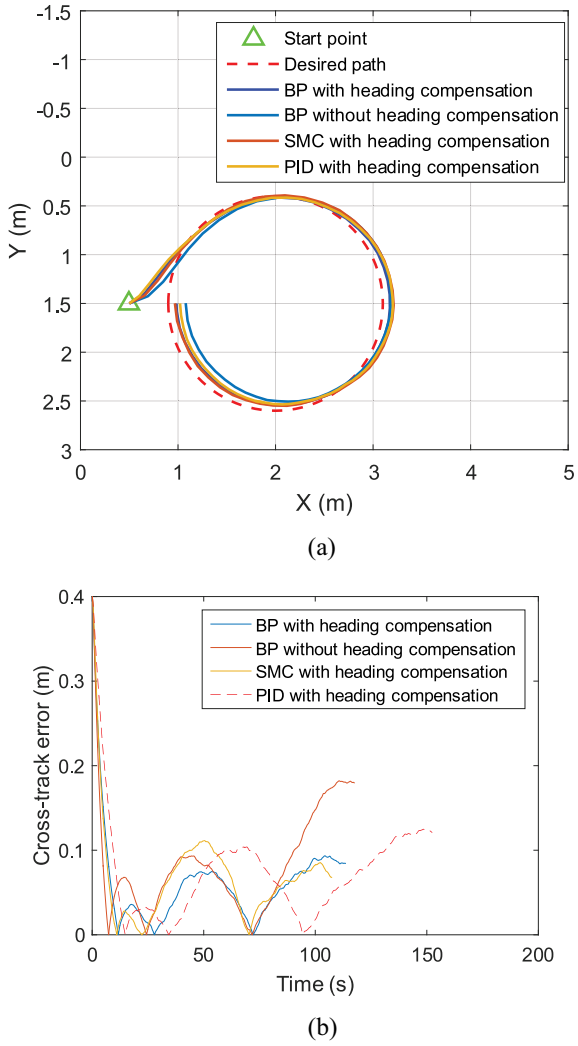

Fig. 9. Comparative simulation results. (a) Desired path and actual path. (b) Cross-track error.

TABLE IV
CONTROLLER PARAMETERS IN THE STRAIGHT PATH FOLLOWING EXPERIMENT

k_1	k_2	k_3	k_4	γ	δ	n	c_0	c_1
0.12	1.8	50	7	0.6	0.04	1	1.5	1

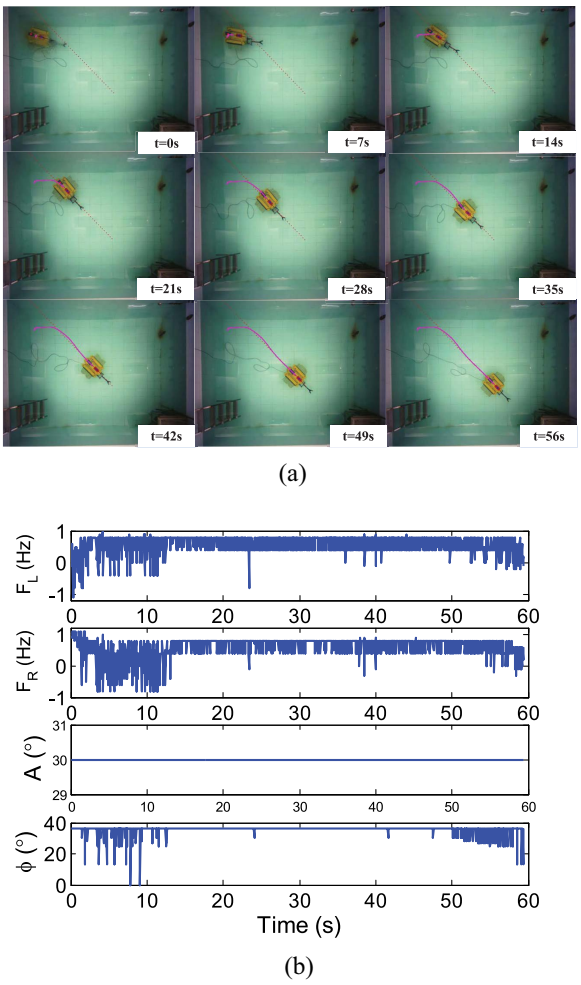

Fig. 10. Experimental results. (a) Image sequence of the straight-line path following. (b) Control parameters of propagating waves on bilateral fins.

error of the proposed method is better than those of the SMC and PID control. When the RobCutt-II moves along the circle, the maximum cross-track error of the SMC and PID with heading compensation are 0.1114 and 0.1249 m, respectively.

Furthermore, some comparative experiments including BP with no heading compensation, SMC [42], and PID control are performed. Fig. 9 shows the simulation results. Specially, the path following can all be achieved as shown in Fig. 9(a). However, it can be seen from Fig. 9(b) that the cross-track error (the shortest distance from the current barycenter of the RobCutt-II to the desired path) of BP with heading compensation is smaller than that of BP without heading compensation in the path following. Specifically, when the RobCutt-II moves along the circle, the maximum cross-track error of the BP with heading compensation is 0.0933 m, while that of the BP without heading compensation is 0.1821 m, which indicates that heading compensation leads to more precise motion than direct calculation of the orientation for path following of the RobCutt-II. Moreover, the cross-track error of the BP is better than those of the SMC and PID control. Specifically, when the RobCutt-II moves along the circle, the maximum cross-track errors of the SMC and PID with heading compensation are 0.1114 and 0.1249 m, respectively.

B. Experimental Results

In order to further evaluate the performance of the proposed control system of the RobCutt-II, straight line and circular path following experiments are performed in an indoor pool with dimensions of 5 m × 4 m × 1.1 m (length × width × depth). The real-time position (x, y) and orientation ψ of the RobCutt-II for closed-loop feedback are obtained based on the global visual tracking system. Specifically, by processing the image information of the RobCutt-II and its surroundings captured by the global visual tracking system, the remote console calculates the position and heading of the RobCutt-II, which are further transmitted to the internal controller of RobCutt-II in real-time.

1) Straight Path Following: A straight line path following experiment is first carried out. The desired path is

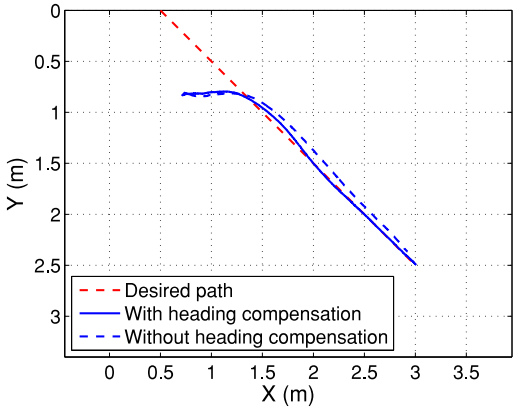

(a)

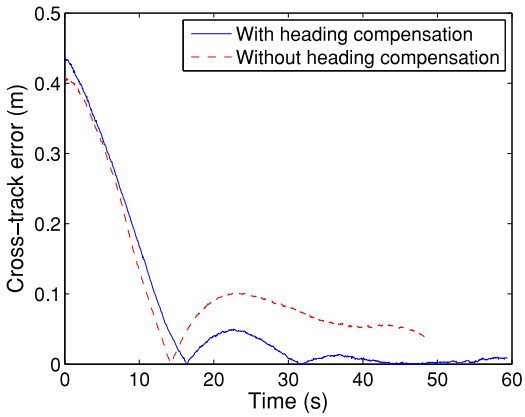

(b)

Fig. 11. Comparative experiment results of straight path following. (a) Desired path and actual path. (b) Cross-track errors.

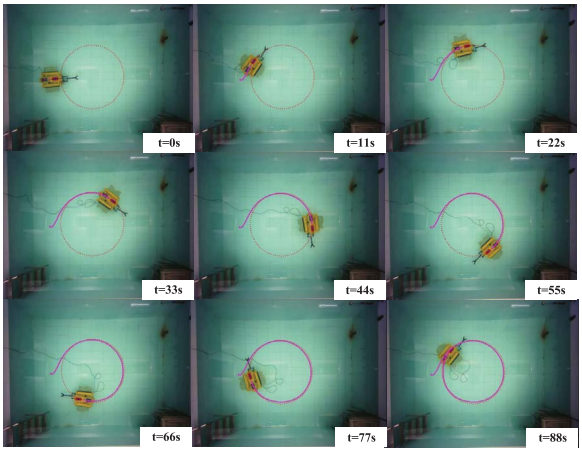

(a)

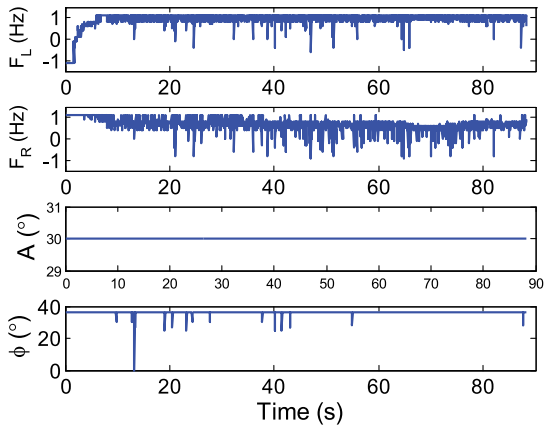

(b)

Fig. 12. Experimental results. (a) Image sequence of the circular path following experiment. (b) Control parameters of propagating waves on bilateral fins.

the same as the simulation. While the initial states of the RobCutt-II are $(x_0, y_0, \psi_0) = (0.720\,\text{m}, 0.836\ \text{m}, 0.250\,\text{rad})$ and $(u_0, v_0, r_0) = (0.017\,\text{m/s}, 0.037\,\text{m/s}, -0.128\,\text{rad/s})$. The parameter settings (listed in Table IV) can be quickly obtained based on the experience of simulations.

Notice that the indoor pool is not large enough to remove the effects of the reflective waves at present, such that the RobCutt-II is subjecting to external disturbances when it swims in the pool.

Fig. 10 shows the experimental results of the straight line path following. The clip of path following experiment is depicted in Fig. 10(a), where the red dotted line is the path to be followed and the pink curve indicates the trajectory of the RobCutt-II. It is observed that the proposed path following control system is able to force the RobCutt-II to catch up and land on the desired path smoothly with small overshoot. Then, the RobCutt-II moves along the desired path and the cross-track error between the desired path and the actual trajectory is small. Fig. 10(b) shows the time evolution of the control parameters of propagating waves on bilateral fins. Notice that the amplitudes of the bilateral long fins maintain at 30° and the turning motion of the RobCutt-II is realized by regulating different frequency of two long fins. In the initial stage of path following, the frequency difference is relatively large to achieve rapid turn, while the frequency difference becomes small during the period of keeping straight with a certain heading.

Furthermore, a comparative experiment in which no heading compensation is added to the controller is performed. Fig. 11(a) shows the desired path and actual path of the RobCutt-II. It is observed that the convergences of the cross-track errors can be achieved in both cases as shown in Fig. 11(b). However, the cross-track error with heading compensation is significantly smaller than that without heading compensation.

2) Circular Path Following: Another experiment is to follow a circular path. The initial position and heading angle of the RobCutt-II are $(0.828\ \text{m}, 2.080\ \text{m})$ and 6.20 rad, respectively, while the initial velocity is $(0.012\ \text{m/s}, -0.008\ \text{m/s}, 0.113\ \text{rad/s})$. Table V shows the parameter settings of the path following controller. Specially, we reduce the radius of the virtual circle γ to reduce the tracking error. Other parameters are also fine-tuned accordingly. The other settings are the same as those of the circular path simulation.

Fig. 12(a) gives the image sequence of the circular path following experiment. The RobCutt-II converges to the circular path and moves along the desired path. Fig. 12(b) shows the

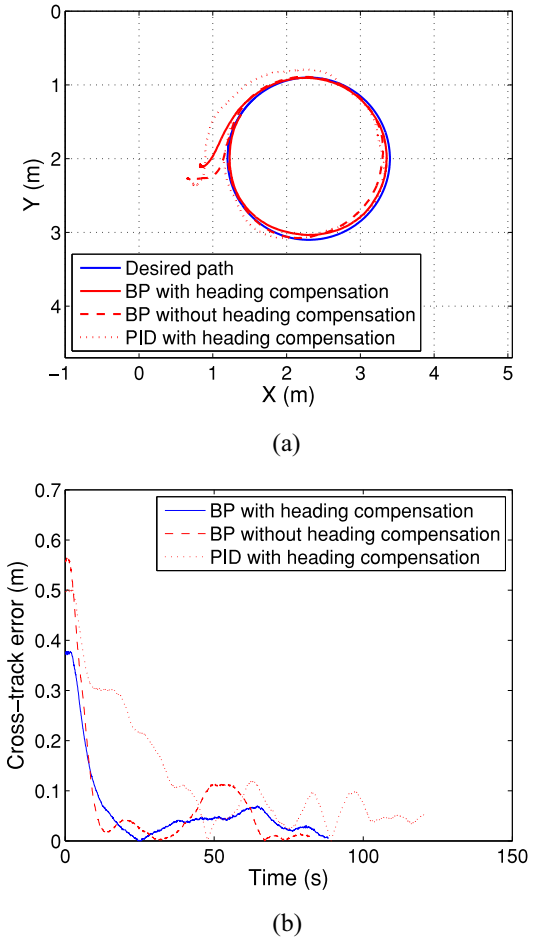

Fig. 13. Comparative experiment results of circular path following. (a) Desired path and actual path. (b) Cross-track errors.

TABLE V
CONTROLLER PARAMETERS IN THE CIRCULAR PATH FOLLOWING EXPERIMENT

k_1	k_2	k_3	k_4	γ	δ	n	c_0	c_1
0.7	2.1	50	5	0.45	0.04	1	1	0.95

parameter settings of propagating waves on bilateral fins. Note that the frequency difference is always large to achieve stable turning maneuver. The amplitude is still kept at 30°. This value can be changed in the following study to realize 3-D motion control.

Furthermore, we evaluate the proposed method with the typical PID controller, where F_L+F_R is used for surge speed control and F_L-F_R is used for heading angle control. The PID parameters are carefully adjusted and the experimental results are shown in Fig. 13. Two kinds of methods can all catch up and follow the desired path. However, the BP method achieves faster convergence to the desired path than the PID method. Moreover, compared with PID method, the proposed controller has a smaller tracking error. Specifically, the maximum cross-track error of the proposed method after the RobCutt-II converges to the desired path is 0.07 m, while the maximum tracking errors are 0.113 and 0.121 m, respectively, using the proposed method without heading compensation and the PID method. It can be concluded that the proposed path following control paradigm is more accurate and effective.

VI. CONCLUSION

In this paper, we have proposed a control paradigm for path following of the RobCutt-II, which was designed to imitate the unique propulsion mode of the cuttlefish. With the coordinated control of the propagating waves on bilateral fins, the RobCutt-II can perform diversified locomotion patterns in water. In order to realize path following, the models of the RobCutt-II, including kinematics/dynamics models and modeling of the biologically inspired propulsor based on fuzzy inference have been developed. Furthermore, a closed-loop control paradigm integrating LOS guidance system with BP technology has been presented for the RobCutt-II path following control. The experimental results show that the BUV is able to autonomously follow straight line and circular paths in the underwater space. Moreover, compared with traditional PID method, the proposed method reduces the cross-track error with a more satisfactory path following result. Meanwhile, the proposed method has stronger disturbance rejection performance due to heading compensation.

Future research will concentrate on the 3-D path-following control and the coordinated motion control of the vehicle-manipulator system.

REFERENCES

[1] D. Blidberg, "The development of autonomous underwater vehicles (AUV); a brief summary," in *Proc. Int. Conf. Robot. Autom. (ICRA)*, Seoul, South Korea, May 2001. [Online]. Available: http://www.ausi.org/publications/ICRA_01paper.pdf
[2] N. Ranganathan, M. Patel, and R. Sathyamurthy, "An intelligent system for failure detection and control in an autonomous underwater vehicle," *IEEE Trans. Syst., Man, Cybern. A, Syst., Humans*, vol. 31, no. 6, pp. 762–767, Nov. 2001.
[3] L. Stutters, H. Liu, C. Tiltman, and D. J. Brown, "Navigation technologies for autonomous underwater vehicles," *IEEE Trans. Syst., Man, Cybern. C, Appl. Rev.*, vol. 38, no. 4, pp. 581–589, Jul. 2008.
[4] K. Alam, T. Ray, and S. G. Anavatti, "Design optimization of an unmanned underwater vehicle using low- and high-fidelity models," *IEEE Trans. Syst., Man, Cybern., Syst.*, to be published.
[5] R. Cui, C. Yang, Y. Li, and S. Sharma, "Adaptive neural network control of AUVs with control input nonlinearities using reinforcement learning," *IEEE Trans. Syst., Man, Cybern., Syst.*, vol. 47, no. 6, pp. 1019–1029, Jun. 2017.
[6] J. Yu, M. Tan, S. Wang, and E. Chen, "Development of a biomimetic robotic fish and its control algorithm," *IEEE Trans. Syst., Man, Cybern. B, Cybern.*, vol. 34, no. 4, pp. 1798–1810, Aug. 2004.
[7] I. D. Neveln *et al.*, "Biomimetic and bio-inspired robotics in electric fish research," *J. Exp. Biol.*, vol. 216, no. 13, pp. 2501–2514, 2013.
[8] M. A. Maciver, E. Fontaine, and J. W. Burdick, "Designing future underwater vehicles: Principles and mechanisms of the weakly electric fish," *IEEE J. Ocean. Eng.*, vol. 29, no. 3, pp. 651–659, Jul. 2004.
[9] M. Sfakiotakis, D. M. Lane, and B. J. Davies, "An experimental undulating-fin device using the parallel bellows actuator," in *Proc. Int. Conf. Robot. Autom.*, Seoul, South Korea, May 2001, pp. 2356–2362.
[10] R. Ruiz-Torres, O. M. Curet, G. V. Lauder, and M. A. Maclver, "Kinematics of the ribbon fin in hovering and swimming of the electric ghost knifefish," *J. Exp. Biol.*, vol. 216, no. 5, pp. 823–834, 2013.
[11] C. Zhou and K. H. Low, "Design and locomotion control of a biomimetic underwater vehicle with fin propulsion," *IEEE/ASME Trans. Mechatronics*, vol. 17, no. 1, pp. 25–35, Feb. 2012.
[12] M. M. Rahman *et al.*, "Braking performance of a biomimetic squid-like underwater robot," *J. Bionic Eng.*, vol. 10, no. 3, pp. 265–273, 2013.
[13] Q. P. Wei, S. Wang, Y. Wang, C. Zhou, and M. Tan, "Course and depth control for a biomimetic underwater vehicle—RobCutt-I," *Int. J. Offshore Polar Eng.*, vol. 25, no. 2, pp. 81–87, 2015.

[14] M. Aureli, V. Kopman, and M. Porfiri, "Free-locomotion of underwater vehicles actuated by ionic polymer metal composites," *IEEE/ASME Trans. Mechatronics*, vol. 15, no. 4, pp. 603–614, Aug. 2010.
[15] G. Karthigan, G. S. Mukherjee, and R. Ganguli, "Electromechanical dynamics and optimization of pectoral fin-based ionic polymer-metal composite underwater propulsor," *J. Intell. Mater. Syst. Struct.*, vol. 23, no. 10, pp. 1069–1082, 2012.
[16] W. He, A. O. David, Z. Yin, and C. Sun, "Neural network control of a robotic manipulator with input deadzone and output constraint," *IEEE Trans. Syst., Man, Cybern., Syst.*, vol. 46, no. 6, pp. 759–770, Jun. 2016.
[17] J. Ghommam and F. Mnif, "Coordinated path-following control for a group of underactuated surface vessels," *IEEE Trans. Ind. Electron.*, vol. 56, no. 10, pp. 3951–3963, Oct. 2009.
[18] A. Aguiar and J. Hespanha, "Trajectory-tracking and path-following of underactuated autonomous vehicles with parametric modeling uncertainty," *IEEE Trans. Autom. Control*, vol. 52, no. 8, pp. 1362–1379, Aug. 2007.
[19] T. I. Fossen, K. Y. Pettersen, and R. Galeazzi, "Line-of-sight path following for Dubins paths with adaptive sideslip compensation of drift forces," *IEEE Trans. Control Syst. Technol.*, vol. 23, no. 2, pp. 820–827, Mar. 2015.
[20] M. E. Serrano, G. J. E. Scaglia, S. A. Godoy, V. Mut, and O. A. Ortiz, "Trajectory tracking of underactuated surface vessels: A linear algebra approach," *IEEE Trans. Control Syst. Technol.*, vol. 22, no. 3, pp. 1103–1111, May 2014.
[21] G. Antonelli, F. Caccavale, and S. Chiaverini, "Adaptive tracking control of underwater vehicle-manipulator systems based on the virtual decomposition approach," *IEEE Trans. Robot. Autom.*, vol. 20, no. 3, pp. 594–602, Jun. 2004.
[22] D. A. Smallwood and L. L. Whitcomb, "Model-based dynamic positioning of underwater robotic vehicles: Theory and experiment," *IEEE J. Ocean. Eng.*, vol. 29, no. 1, pp. 169–186, Jan. 2004.
[23] E. Børhaug, A. Pavlov, E. Panteley, and K. Y. Pettersen, "Straight line path following for formations of underactuated marine surface vessels," *IEEE Trans. Control Syst. Technol.*, vol. 19, no. 3, pp. 493–506, May 2011.
[24] A. J. Healey and D. Lienard, "Multivariable sliding mode control for autonomous diving and steering of unmanned underwater vehicles," *IEEE J. Ocean. Eng.*, vol. 18, no. 3, pp. 327–339, Jul. 1993.
[25] B. Sun, D. Zhu, and S. X. Yang, "A bioinspired filtered backstepping tracking control of 7000-m manned submarine vehicle," *IEEE Trans. Ind. Electron.*, vol. 61, no. 7, pp. 3682–3693, Jul. 2014.
[26] K. D. Do, Z. P. Jiang, and J. Pan, "Robust adaptive path following of underactuated ships," *Automatica*, vol. 40, no. 6, pp. 929–944, 2004.
[27] L. Lapierre and B. Jouvencel, "Robust nonlinear path-following control of an AUV," *IEEE J. Ocean. Eng.*, vol. 33, no. 2, pp. 89–102, Apr. 2008.
[28] X. Liang, L. Wan, J. I. R. Blake, R. A. Shenoi, and N. Townsend, "Path following of an underactuated AUV based on fuzzy backstepping sliding mode control," *Int. J. Adv. Robot. Syst.*, vol. 13, no. 3, p. 122, 2016.
[29] R.-J. Lian, "Intelligent controller for robotic motion control," *IEEE Trans. Ind. Electron.*, vol. 58, no. 11, pp. 5220–5230, Nov. 2011.
[30] J. Guo, F.-C. Chiu, and C.-C. Huang, "Design of a sliding mode fuzzy controller for the guidance and control of an autonomous underwater vehicle," *Ocean Eng.*, vol. 30, no. 16, pp. 2137–2155, 2003.
[31] Z. Liu, B. Chen, and C. Lin, "Adaptive neural backstepping for a class of switched nonlinear system without strict-feedback form," *IEEE Trans. Syst., Man, Cybern., Syst.*, to be published.
[32] H. Liu, Y. Pan, S. Li, and Y. Chen, "Adaptive fuzzy backstepping control of fractional-order nonlinear systems," *IEEE Trans. Syst., Man, Cybern., Syst.*, to be published.
[33] Y. Wang *et al.*, "Development of an underwater manipulator and its free-floating autonomous operation," *IEEE/ASME Trans. Mechatronics*, vol. 21, no. 2, pp. 815–824, Apr. 2016.
[34] R. Wang and S. Wang, "Design and implementation of a biomimetic underwater propeller with a undulating long fin," *J. Huazhong Univ. Sci. Technol. (Nat. Sci. Ed.)*, vol. 43, no. s1, pp. 408–411, 2015.
[35] R. Wang, S. Wang, and Y. Wang, "A hybrid heading control scheme for a biomimetic underwater vehicle," in *Proc. 26th Int. Ocean Polar Eng. Conf.*, Rhodes, Greece, Jun. 2016, pp. 619–625.
[36] T. I. Fossen, *Guidance and Control of Ocean Vehicles*. New York, NY, USA: Wiley, 1994.
[37] "Nomenclature for treating the motion of a submerged body through a fluid," in *Technical and Research Bulletin*. New York, NY, USA: Soc. Naval Archit. Marine Eng., 1952, pp. 1–5.
[38] F. Liu, C.-J. Yang, and K.-M. Lee, "Hydrodynamic modeling of an undulating fin for robotic fish design," in *Proc. IEEE/ASME Int. Conf. Adv. Intell. Mechatronics*, Montreal, QC, Canada, Jul. 2010, pp. 55–60.
[39] A. A. Shirgaonkar, O. M. Curet, N. A. Patankar, and M. A. MacIver, "The hydrodynamics of ribbon-fin propulsion during impulsive motion," *J. Exp. Biol.*, vol. 211, no. 21, pp. 3490–3503, 2008.
[40] Q.-P. Wei, S. Wang, X. Dong, L.-J. Shang, and M. Tan, "Design and kinetic analysis of a biomimetic underwater vehicle with two undulating long-fins," *Acta Automatica Sinica*, vol. 39, no. 8, pp. 1330–1338, 2013.
[41] A. M. Lyapunov, "The general problem of the stability of motion," *Int. J. Control*, vol. 55, no. 3, pp. 531–534, 1992.
[42] J. Liu, *Sliding Mode Control Design and MATLAB Simulation*. Beijing, China: Tsinghua Univ. Press, 2012.

Rui Wang received the B.E. degree in automation from the Beijing Institute of Technology, Beijing, China, in 2013. He is currently pursuing the Ph.D. degree in control theory and control engineering with the State Key Laboratory of Management and Control for Complex Systems, Institute of Automation, Chinese Academy of Sciences, Beijing.

He is with the University of Chinese Academy of Sciences, Beijing. His current research interests include intelligent control, robotics, and biomimetic robots.

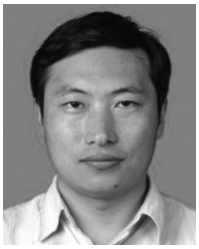

Shuo Wang received the B.E. degree in electrical engineering from the Shenyang Architecture and Civil Engineering Institute, Shenyang, China, in 1995, the M.E. degree in industrial automation from Northeastern University, Shenyang, in 1998, and the Ph.D. degree in control theory and control engineering from the Institute of Automation, Chinese Academy of Sciences, Beijing, China, in 2001.

He is currently a Professor with the State Key Laboratory of Management and Control for Complex Systems, Institute of Automation, Chinese Academy of Sciences. His current research interests include biomimetic robot, underwater robot, and multirobot systems.

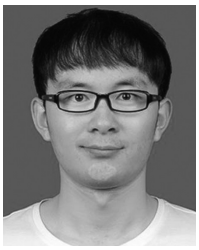

Yu Wang received the B.E. degree from the Beijing Institute of Technology and the Ph.D. degree in control theory and control engineering from the Institute of Automation, Chinese Academy of Sciences, Beijing, China, in 2011 and 2016, respectively.

He is currently a Research Assistant with the State Key Laboratory of Management and Control for Complex Systems, Institute of Automation, Chinese Academy of Sciences. His current research interests include intelligent control, robotics, and biomimetic robots.

Min Tan received the B.E. degree from Tsinghua University, Beijing, China, in 1986 and the Ph.D. degree in control theory and control engineering from the Institute of Automation, Chinese Academy of Sciences, Beijing, in 1990.

He is currently a Professor with the State Key Laboratory of Management and Control for Complex Systems, Institute of Automation, Chinese Academy of Sciences. His current research interests include advanced robot control, biomimetic robot, and multirobot system.

Junzhi Yu (SM'14) received the B.E. degree in safety engineering and the M.E. degree in precision instruments and mechanology from the North China Institute of Technology, Taiyuan, China, in 1998 and 2001, respectively, and the Ph.D. degree in control theory and control engineering from the Institute of Automation, Chinese Academy of Sciences (IACAS), Beijing, China, in 2003.

He is currently a Professor with the State Key Laboratory of Management and Control for Complex Systems, IACAS. His current research interests include biomimetic robots, intelligent control, and intelligent mechatonic systems.

Dr. Yu serves as the Associate Editor of the IEEE TRANSACTIONS ON ROBOTICS and the *Journal of Mechanical Science and Technology*, and as a Technical Editor of the IEEE/ASME TRANSACTIONS ON MECHATRONICS.